APPLIED SCIENCES AND ENGINEERING

Underwater metamaterial absorber with impedance-matched composite

Sichao Qu[1]†, Nan Gao[1]†, Alain Tinel[2], Bruno Morvan[2], Vicente Romero-García[3], Jean-Philippe Groby[3], Ping Sheng[1]*

By using a structured tungsten-polyurethane composite that is impedance matched to water while simultaneously having a much slower longitudinal sound speed, we have theoretically designed and experimentally realized an underwater acoustic absorber exhibiting high absorption from 4 to 20 kHz, measured in a 5.6 m by 3.6 m water pool with the time-domain approach. The broadband functionality is achieved by optimally engineering the distribution of the Fabry-Perot resonances, based on an integration scheme, to attain impedance matching over a broad frequency range. The average thickness of the integrated absorber, 8.9 mm, is in the deep subwavelength regime (~λ/42 at 4 kHz) and close to the causal minimum thickness of 8.2 mm that is evaluated from the simulated absorption spectrum. The structured composite represents a new type of acoustic metamaterials that has high acoustic energy density and promises broad underwater applications.

INTRODUCTION

Underwater acoustics represents an area of study that is important for the subsurface exploration and object imaging in rivers and oceans that occupy the majority of Earth's surface. The efficient absorption of low-frequency underwater acoustic waves has especially attracted strong interest, notably for the applications in underwater sensing and stealth technologies (*1*–*3*). Despite its apparent importance, however, this topic is nowhere as intensely pursued as either airborne audible sound (*4*–*7*) or ultrasound (*8*–*10*). The latter represents the higher-frequency branch of the waterborne acoustic waves that has found widespread use in medical applications. One reason for this state of affairs is the difficulty of experimental measurements, owing to the large wavelength involved and the required large impedance mismatch of the solid material for a water impedance tube (*11*, *12*). As a result, considerable studies on underwater absorption are only limited to theoretical analyses and numerical calculations (*13*–*22*), whose idealized assumptions may not hold in practical scenarios, while almost all the existing experimental works (*23*–*30*), measured in the water impedance tube, are based on small samples, which may not reflect the true performance in complex environments (*31*). There is simply a lack of research works based on large-scale samples, measured in water pools. Besides the experimental obstacles, designing an underwater absorber itself can be a challenge for theoretical modeling, because of the diversity of solid elastic vibration modes (*32*) that can give rise to difficulty in focusing on the absorption functionality absent of any undesired features. In addition, the acoustic energy density of the conventional materials (*33*, *34*) for underwater applications is relatively low, which hinders the efficient dissipation of the low-frequency waves within an acoustically thin sample. In other words, the potential of reducing the thickness of the underwater absorber has not yet been fully explored.

[1]Department of Physics, The Hong Kong University of Science and Technology, Clear Water Bay, Kowloon, Hong Kong, China. [2]Laboratoire Ondes et Milieux Complexes UMR CNRS 6294, UNILEHAVRE, Normandie University, 75 Rue Bellot, 76600 Le Havre, France. [3]Laboratoire d'Acoustique de l'Université du Mans (LAUM), UMR 6613, Institut d'Acoustique—Graduate School (IA-GS), CNRS, Le Mans Université, Le Mans, France.
*Corresponding author. Email: sheng@ust.hk
†These authors contributed equally to this work.

In this work, we present a novel metamaterial absorber with structured impedance-matched composite, which can offer a solution to the aforementioned challenges in underwater absorption. Our composite comprises tungsten particles dispersed in a polyurethane (PU) polymer matrix, geometrically structured into slender rods, thereby enabling to treat them as one-dimensional solids. As the longitudinal speed in a rod is governed by its Young's modulus E_c, for the PU matrix, it can be easily tuned to be lower than the bulk modulus of water B_w. Meanwhile, the dispersed tungsten particles can contribute to a considerably larger mass density ρ_c than that of water, ρ_w. It follows that the characteristic impedance of our structured composite can be easily tuned to match that of water. Simultaneously, such a composite material would have a much slower longitudinal wave speed than that in water, thereby implying a larger acoustic density of states at low frequencies. As a result, when the rods are backed by a hard reflecting boundary, the Fabry-Pérot (FP) resonances can be realized with a much thinner thickness than that of the conventional materials.

In what follows, we delineate the process of synthesizing tungsten-PU composite to attain the desired properties. To achieve broadband impedance matching, we use an integration scheme of multiple FP resonances and experimentally verify the absorption performance of a 0.92 m by 0.92 m sample in a water pool. It will be shown that good agreement between the simulation and experiment is obtained, with an average absorption over 90% from 4 to 20 kHz and an average sample thickness of only 8.9 mm, which is close to the minimum sample thickness as dictated by the causality constraint (*5*).

RESULTS

The impedance-matching composite and slow sound effect

We introduce a dimensionless scaling factor α (α > 1) to simultaneously tune the following parameters of the composite rod—the density ρ_c and the longitudinal modulus M

$$\rho_c \to \alpha\rho_w, M \to \frac{B_w}{\alpha} \quad (1)$$

where the water density $\rho_w = 1$ g/cm^3 and bulk modulus $B_w = 2.16 \times 10^9$ Pa. In this manner, the composite's characteristic acoustic impedance $\sqrt{\rho_c M}$ is matched with that of water $\sqrt{\rho_w B_w}$. In addition, the sound speed in the composite will be slower, i.e., $v_c = \sqrt{\frac{M}{\rho_c}} = \frac{1}{\alpha}\sqrt{\frac{B_w}{\rho_w}} = \frac{v_w}{\alpha}$, while the wavelength is compressed as well, i.e., $\lambda = \frac{v_w}{\alpha f} = \frac{\lambda_w}{\alpha}$. We treat the slender composite rod as one-dimensional solid materials since its length L is longer than its lateral size a = 5 mm. Therefore, the longitudinal modulus M can be approximated as Young's modulus E_c of the composite rod with the free boundary condition on the four sidewalls of the rod and rigid backing condition at the bottom (Fig. 1A). This can be evidenced by the simulation based on finite-element method (FEM), where we evaluate the displacement of the upper surface of the rod ΔL, under a static pressure modulation Δp. We directly set the Young's modulus $E_c = B_w/\alpha$ and compare it with the retrieved effective longitudinal modulus, given by $M = L\Delta p/\Delta L$. The simulation results, displayed in Fig. 1B, confirm the one-dimensional model assumption, because $M \cong E_c$ for all values of α.

If we launch a harmonic plane wave onto the composite rod (Fig. 1A), the FP resonance (*5*) will occur when a quarter wavelength is equal to the rod length L. Here, by fixing f to be the target frequency, the length of the FP rod L is proportional to the sound speed in composite materials, with $L = \frac{v_c}{4f} = \frac{v_w}{4\alpha f} = \frac{L_0}{\alpha}$. This indicates that by using slow sound materials ($\alpha > 1$), we can reduce the FP resonator's length without changing the resonant frequency. Furthermore, we investigate the surface response spectrum as characterized by the Green function (*6*, *35*), defined by averaged displacement x/pressure modulation p, at the top surface of the rod. As an example, we choose the target frequency f = 3.5 kHz, with L_0 = 0.1 m. It is seen that when the parameters are scaled as in Eq. 1 with α = 1 or 5.5, the relevant Green function, $G(\omega)$, plotted as a function of frequency in Fig. 1 (C and D), remains exactly the same for the two cases as evidenced by the complete overlap of the blue continuous and red dashed lines. In other words, at the theoretical level, there exists an opportunity that the same surface response can be supported with a much shorter length, $L = L_0/\alpha$, when α is large. In the following section, we show such material properties with α = 5.5 given in Eq. 1 can be realized experimentally.

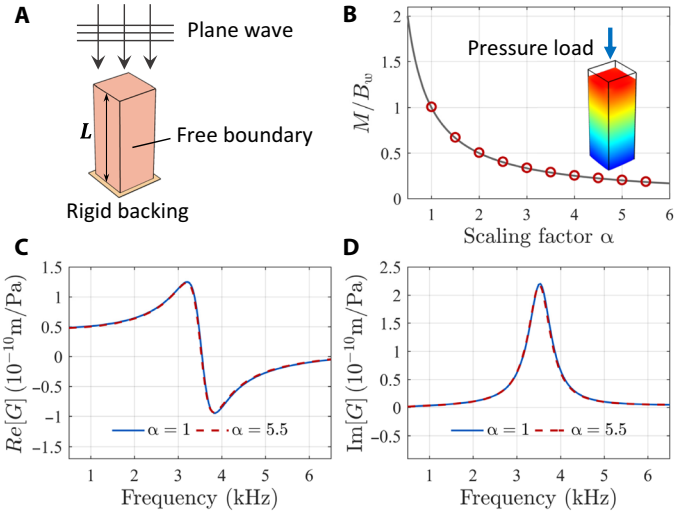

Fig. 1. The composite rod with tunable modulus. (**A**) Schematic of the single FP resonator made by a composite rod. (**B**) Effective modulus of the composite rod as function of the scaling factor α. The solid line denotes the Young's modulus $E_c = B_w/\alpha$ specified in the simulation, while the circles denote the effective longitudinal modulus, retrieved from the simulated output data. The inset figure shows the displacement field under the pressure load Δp. (**C**) Real part of the Green function, $G(\omega)$, with α = 1 and 5.5. The data are retrieved from simulations. The complete overlap of the two curves shows that the Green function is independent of the scaling parameter α. (**D**) Same for the imaginary part of the Green function.

Tuning the composite's acoustic properties

We target a composite with high acoustic energy density as specified by α = 5.5. In the literature, an impedance-matched material is usually denoted as "Rho-C rubber" (*1*, *36*, *37*), which usually means that both the material's density and sound speed are close to those of water. However, for our structured composite rods, while the effective impedance can be matched to that of water, the wave speed is slower and the acoustic energy density (*38*) is α times higher, given by

$$\varepsilon = \frac{1}{2}\rho_c v^2 + \frac{1}{2}\frac{1}{M}p^2 = \alpha\left(\frac{1}{2}\rho_w v^2 + \frac{1}{2}\frac{1}{B_w}p^2\right) \quad (2)$$

where p and v denote the acoustic pressure modulation and the particle displacement velocity, respectively, and the term in the bracket is the energy density in water or the Rho-C rubber.

The ingredients for synthesizing the composite are tungsten granules (W), uniformly dispersed in PU polymer (Fig. 2A). Here, the PU polymer was composed of a softer PU rubber and a harder PU resin (Fig. 2B). The tungsten, with its density of 19.3 g/cm^3, was used for the purpose of creating a composite with large density, while the PU polymer was chosen for low and tunable modulus. The total mass of the composite is the summation of all the ingredients

$$\begin{cases} M_{total} = M_{PU} + M_W = (R_1 + 1)M_W, \\ M_{PU} = M_{resin} + M_{rubber} = (R_2 + 1)M_{rubber} \end{cases} \quad (3)$$

where $R_1 = M_{PU}/M_W$, $R_2 = M_{resin}/M_{rubber}$, and the subscript "W" denotes tungsten.

We show that by tuning R_1 and R_2 in two steps, the target density and longitudinal modulus can be attained. We first mixed tungsten granules with PU resin and PU rubber separately ($\rho_{resin} = \rho_{rubber} \cong 1$ g/cm^3). Since the density of PU rubber is the same as PU resin, the outcome of the mixed gels coincides when the ratio between the PU polymer and tungsten is the same (Fig. 2C). By adjusting the ratio of tungsten to be R_1 = 0.0145, we obtained ρ_c = 5.5 g/cm^3 = 5.5 ρ_w. Next, by fine-tuning the ratio R_2, we manipulated the Young's modulus of the composite without changing the density. It turned out that if R_2 = 0.524 (Fig. 2D), the resulting modulus $E_c = 0.37 \times 10^9$ Pa $\cong B_w/5.5$ (Fig. 2E). In this manner, we realized the composite with a high mass density and low bulk modulus while keeping the impedance matched to that of water, i.e., $\sqrt{\rho_c E_c} = \sqrt{\rho_w B_w}$. Theoretically, the target α can be higher than 5.5, as long as we are still working below the percolation threshold (*35*) of the tungsten granules. However, to ensure the uniformity of the composite sample, α = 5.5 was fixed for the subsequent theoretical design and sample fabrication.

FP resonators and the integration scheme for broadband absorption

The FP resonator used in this work is simply a slender solid rod with a rigid reflecting boundary at the bottom end. The resonance

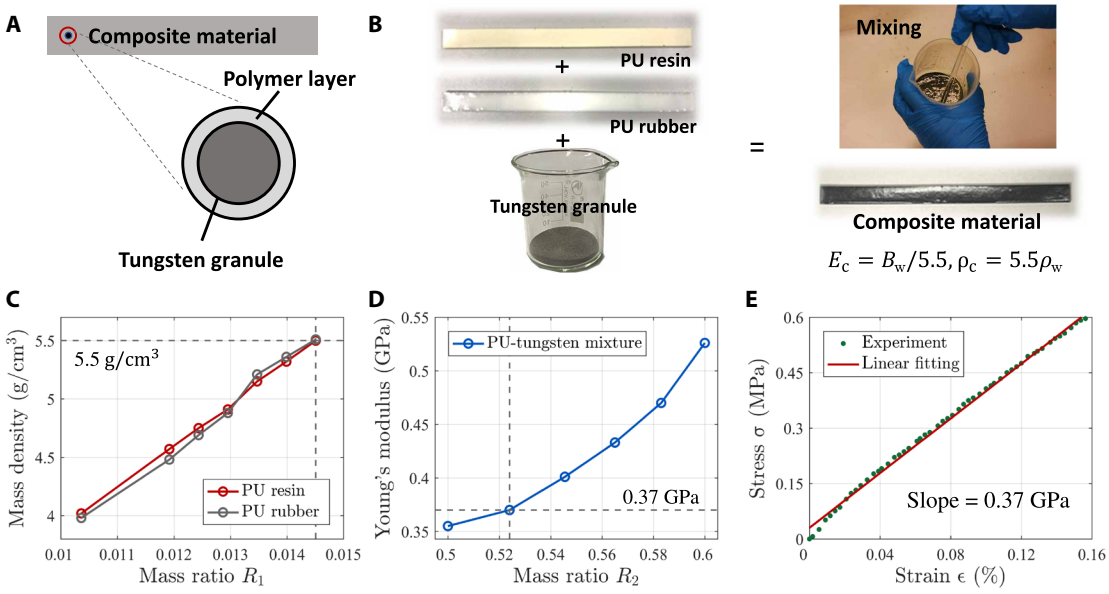

Fig. 2. The composite fabrication process for targeting α=5.5 and its verification. (**A**) Schematic illustration of the composite material's microstructure, comprising tungsten granules embedded in a polymer matrix. (**B**) By mixing PU resin, PU rubber, and tungsten granules, we fabricate the composite material with the targeted properties, whose final stripe shape is used for the tensile test. (**C**) Relation between the mass density and the mass ratio $R_1 = M_{PU}/M_W$, for which M_{PU} can be contributed by either varying PU resin (red) or PU rubber (gray). (**D**) By fixing the mass ratio R_1, we change the mass ratio R_2 between the PU resin and PU rubber (i.e., $R_2 = M_{resin}/M_{rubber}$) to manipulate sample's Young's modulus. (**E**) Measured strain-stress curve for the final composite sample, showing its Young's modulus $E \cong 0.37 \times 10^9$ Pa, the target longitudinal modulus of the rod.

condition is attained when one-quarter of the relevant wavelength matches the length of the rod. Because the relevant wavelength in the composite rod is much shorter, it follows that the length of the resonators can also be much shorter, thereby leading to a thinner absorber. The lateral size of the resonators is very small relative to the wavelength (i.e., a = 5 mm $\ll \lambda$). Therefore, only the longitudinal modes should be taken into consideration and the surface impedance of the individual n_{th} FP resonator in an integrated array has the simple form $Z_n = iZ_w \cot(\omega L_n/v_c)$. Note that we use the harmonic time dependence of $\exp(-i\omega t)$ throughout our manuscript. The Green function (*6*, *35*), defined as the surface response of n_{th} composite rod, is given by $G_n = u_n/(-i\omega p) = 1/(-i\omega Z_n)$, where u_n denotes the displacement velocity on the upper surface. With some mathematical manipulation (*39*) (see details in the Supplementary Materials, text S1), G_n may be expressed in the Lorentzian form

$$G_n(\omega) \cong \frac{\chi_n}{\Omega_n^2 - \omega^2 - i\beta\omega} \tag{4}$$

where the oscillation strength $\chi_n = 2/(\rho_c L_n) = 2/(\rho_w L_0)$, the resonant angular frequency $\Omega_n = 2\pi f_n = \pi v_c/(2L_n)$, and the factor β is introduced to model the dissipation (details are available in the Supplementary Materials, text S2). We see that Eq. 4 is independent of α, which is consistent with the results shown in Fig. 1 (C and D).

To realize broadband impedance matching, we integrate FP resonators with nine different lengths (L_1, L_2, …, L_9) as a unit cell [see schematic illustration of the resonator integration in Fig. 3 (A and B)]. Earlier works (*5*, *40*) have shown that if we adopt the approximation of ignoring the higher-order FP resonances in each of the resonators, then the optimal choice of the resonance frequencies (f_1, f_2, …, f_9), for yielding a flat, near-total absorption curve is given by the formula $f_n = f_1 e^{2(n-1)/9}$ as plotted in dashed line in Fig. 3C, with the corresponding $L_n = v_c/(4f_n)$. Here, $L_1 = L_0/5.5$ and f_1 = 3.5 kHz. An integration scheme, including the correction due to the higher-order FP resonances in each resonator, is given in the Supplementary Materials, text S3, which yields the resonance distribution slightly different from the first-order power law, as shown by the solid line in Fig. 3C. The final discretized resonances are indicated by the circles in Fig. 3C and arrows in Fig. 3E, leading to the final length recipe to be L_1 = 18.9 mm, L_2 = 15.2 mm, L_3 = 12.2 mm, L_4 = 9.8 mm, L_5 = 7.9 mm, L_6 = 6.4 mm, L_7 = 4.6 mm, L_8 = 3.1 mm, and L_9 = 1.7 mm. It should be noted that while the length is smaller than the lateral size (a = 5 mm) for resonators 7 to 9, simulations have shown the desired scaling characteristics can still hold.

To verify the effect of the integration scheme, we first calculate the averaged surface response of the integrated resonators placed in parallel such that $G_s = \sum_{n=1}^{9} G_n/9$, where G_n is given by Eq. 4. Here, the factor 1/9 denotes the area fraction occupied by each resonator surface facing the incident wavefront. The overall surface impedance of the sample array is given by

$$Z_s(\omega) = \frac{1}{-i\omega G_s} = \left(\frac{1}{9}\sum_{n=1}^{9}\frac{1}{Z_n}\right)^{-1} \tag{5}$$

which is shown by the solid curve in Fig. 3D. In Eq. 5, as an approximation, we have ignored the coupling effects between the adjacent rods (*5*, *6*), through the evanescent waves. It is seen that broadband impedance matching is achieved with the chosen rod lengths. The real part of the impedance is close to Z_w beyond 3.5 kHz, and the imaginary part vanishes as the frequency increases. The absorption coefficient can be obtained by inserting Eq. 5 into the following expression

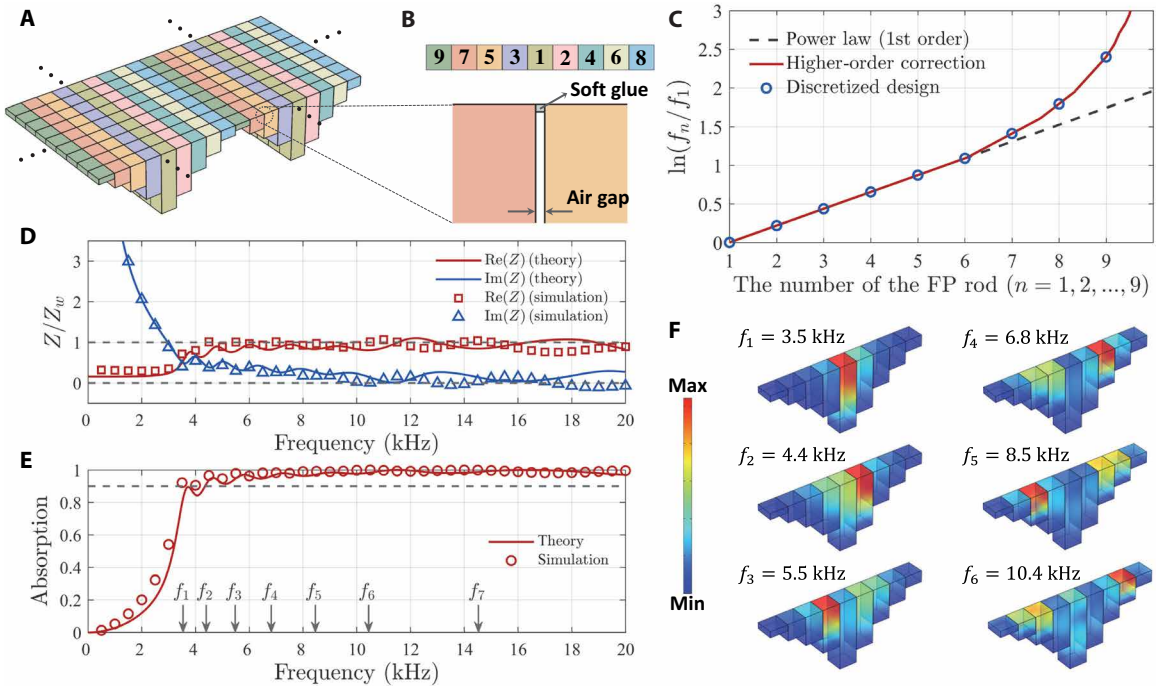

Fig. 3. Integrated FP resonator array for attaining broadband underwater acoustic absorption. (**A**) Schematic of the resonator array. The dots indicate periodic repetition. (**B**) The nine FP resonator lengths, indicated by different colors together with an enlarged view of the air gap between two neighboring rods, with a thin layer of waterproof soft glue adhered on the top surface facing the water. (**C**) Design recipe of the resonance frequency distribution for realizing impedance matching. (**D**) The resulting real and imaginary parts of impedance, plotted as function of frequency. (**E**) The absorption spectrum and the first-order resonance frequencies are indicated by the gray arrows on the horizontal axis. Note that f_8 and f_9 are higher than 20 kHz. (**F**) The simulated velocity fields at different selected resonance frequencies.

$$A(\omega) = 1 - \left|\frac{Z_s - Z_w}{Z_s + Z_w}\right|^2 \tag{6}$$

where the water impedance $Z_w = \sqrt{\rho_w B_w}$. In Fig. 3E, we show the resulting broadband absorption, given by Eq. 6, which starts around 4 kHz (slightly higher than f_1). We also compare the theoretical prediction with that of full-wave FEM simulations, plotted as circles in Fig. 3E. Good agreement between theory predictions and simulations is seen. It should be noted that two neighboring rods are separated by a ~50-μm air gap (Fig. 3B), with the soft water-repellent glue seal on top. The air gap is essentially the average separation between two macroscopically flat surfaces of the two touching objects, owing to the usual amount of surface asperities and microscopic undulations. While there can be multiple contact points of the two surfaces, longitudinal vibration modes in the nearby rods are essentially decoupled from each other. In Fig. 3F, we plot the velocity fields inside the FP resonators from f_1 to f_6. It is not unexpected that at the resonance frequency f_n, the rod with L_n displays the response with largest surface velocity. For the frequencies in between the FP resonances (or higher frequencies beyond f_6), the impedance matching condition is realized as well, but more than one resonator can be excited.

The causality constraint on sample thickness

Because of the fundamental causal nature (*41*–*43*) of an absorber's response to the incident wave, there is a minimum sample thickness associated with any given absorption spectrum $A(\lambda)$. For acoustic systems, this causal constraint takes the form of an inequality (*5*, *6*)

$$\bar{d} \geq d_{\min} = \frac{1}{4\pi^2}\frac{B_{\text{eff}}}{B_w}\int_0^\infty |\ln(1 - A(\lambda))|\, d\lambda \tag{7}$$

where $\bar{d}$ denotes the average thickness of the absorber, and the value of static modulus, $B_{\text{eff}}/B_w \cong E_c/B_w = 1/5.5$ in the present case. The wavelength in water $\lambda = v_w/f$. From Eq. 7, we again see that by using the slow sound medium, the lower bound thickness, $d_{\min}$, can be substantially reduced, which is consistent with the results shown in Fig. 1 (C and D). We can insert the simulated absorption in Fig. 3E into Eq. 7 to obtain $d_{\min}$ = 8.2 mm, which is close to the average thickness ($\bar{d} = \sum_{n=1}^{9} L_n/9$ = 8.9 mm). Hence, at the stage of theoretical design, we conclude that the performance of our absorber has approached the causality limit. Although the causally optimal broadband absorbers have been realized in airborne acoustic (*5*, *6*) and electromagnetic systems (*43*), we demonstrate here that the causal limit can be modified, or more specifically lowered, by using impedance-matched composite with slow-sound properties.

Sample fabrication considerations

As for sample fabrication, we have structured the composite into rod shapes with predesigned lengths by using molds (Fig. 4A). The fabrication procedures of the rods are given in the Supplementary Materials, text S4. Because the FP resonators require a reflecting backing substrate, we have also fabricated a stainless-steel base, with stepped stairs that is complementary to the lengths of the rods, so that the upper surface of the sample is flat (Fig. 4, A and B). The total sample thickness, including the stainless-steel base, was designed to be ~0.069 m so as to greatly reduce the transmission beyond 3.5 kHz. We let neighboring rods come into contact naturally so that there must exist some small amount of air space between the rods. We brushed

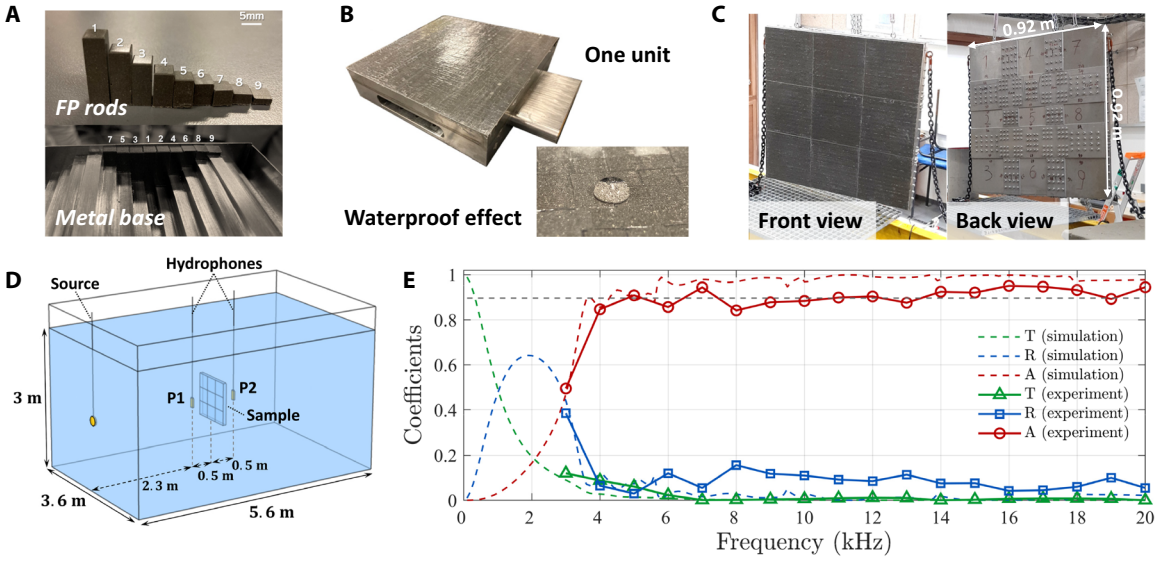

Fig. 4. Experimental realization of the underwater metamaterial absorber with water pool measurement. (**A**) Fabricated composite rods, placed on the stepped stainless-steel base. (**B**) One sample unit and the waterproof effect on the top surface, with the adoption of the soft glue. Water is shown to form a droplet shape because of the hydrophobic effect of the waterproof soft glue. (**C**) Front view and back view of the assembled sample, comprising nine units. (**D**) Schematic of the water pool measurement configuration. (**E**) Measured data with the transmittance T, the reflectance R, and the absorption $A = 1 - T - R$. The results retrieved from simulation are also presented by dashed lines, for comparison. Here, the simulations have taken into account the stainless-steel base.

a thin layer of the hydrophobic soft glue to trap the air and to prevent water from seeping into the gaps (Fig. 4B). Because of the heavy mass of the stainless-steel base, we divided the sample into 3 × 3 units so as to facilitate easy assembly into the whole with a dimension of 0.92 m by 0.92 m (Fig. 4, B and C).

Experimental verification in a water pool

To test the absorption of the sample in an underwater environment, we have carried out the measurements in a water pool with the configuration shown in Fig. 4D. The sample, source, and hydrophone were placed in the middle of the 5.6 m by 3.6 m water pool to minimize the interference of the boundaries. A burst signal was emitted by the directional source, reflected by the sample and received by a hydrophone at two different positions for collecting the reflection and transmission data (plotted in Fig. 4E). To compare with the experimental data, we take into account the stainless-steel base in the simulations (instead of the rigid backing condition) so as to allow some transmission of the incident wave, which is plotted as green dashed lines in Fig. 4E.

In the low-frequency regime below 0.5 kHz, the transmission dominates because of the by-passing effect of the long wavelength. With increasing frequency, reflection appears and reaches its maximum around 2 kHz. If the sample is made of pure stainless steel, the reflection will keep increasing and reach almost unity at higher frequencies, but because of the metastructures on the front side of the sample, the strong reflection turns into the absorption inside the high-energy-density composite. We obtain an averaged absorption (from 4 to 20 kHz) of 97.6% for the simulation and 90.3% for the experiment (Fig. 4E). It should be noted that the averaged sample thickness is only 8.9 mm, which is only 1/42 wavelength at 4 kHz, while for the longest rod, the same value is 1/20. While the measurement results basically validated our design approach, the observable difference between the simulated and measured results may result from the inevitable imperfections in the manufacturing and the assembling of the sample, which were all done manually (refer to the Supplementary Materials, text S4). Such imperfections can mean that the idealized perfect pressure-release boundary was actually not the case in the experimental sample, leading to the weak interactions between adjacent resonators and thereby slightly lower the measured absorption. If automated and accurate mass production can be achieved in the future, we expect such problems to be largely mitigated.

DISCUSSION

By comparing our work with the traditional absorbers, such as the anechoic coatings (*13*, *44*–*47*) and penta-mode structures (*19*), we find that our design scheme is straightforward and more effective because only the longitudinal modes are involved, achieved by both the rod geometry separated by air gaps, and the subwavelength lateral dimension of each rod. In this manner, the lateral modes can only exist in the form of evanescent waves, which cannot couple to the incident wave (*48*). Further simulation shows that smaller lateral size of the rods not only helps improve the higher frequency absorption but also enhances the performance under oblique incidence (*49*) (results are available in the Supplementary Materials, text S5). Unlike the air bubble–based absorber (*10*, *13*, *23*, *47*, *50*), in principle, our absorber does not rely on the resonant modes shaped by air cavities to achieve impedance matching and holds the potential of mitigating the absorption-degrading problem under hydrostatic pressure (i.e., without evident nonlinear deformation of the solids involved). We performed an initial simulation study in the Supplementary Materials, text S6, to check this point and found that the simulated performance does not significantly suffer under hydrostatic pressure. However, we believe that more experiments are needed in the future to fully verify the performance under elevated

pressure, because our sample requires the maintenance of thin air gaps between the resonators, and the associated high demands on the fabrication and assembly technique. Our composite's intrinsic properties also ensure that the slow sound effect holds for the whole frequency spectrum, which differs from the resonance-based slow sound absorber (*51*–*53*), for which the enhanced absorption occurs near the resonant frequencies. As for the absorbing bands, the starting frequency is actually tunable and can be easily shifted down to the lower subkilohertz regime. This can be done by multiplying the current rod lengths by a factor larger than 1 (see absorption results in the Supplementary Materials, text S7). In our experiment, we just measured from 3 to 20 kHz, because of the limitations of the pool size and the performance of the sound sources. However, through simulations, we do not see any reason why our absorber cannot extend to lower and higher frequencies.

In conclusion, our work not only offers an integration scheme for broadband impedance matching but also proposes a novel type of impedance-matched and high-energy-density composite that can realize excellent underwater absorption with thin sample thickness. The former provides a design recipe for solving the narrow band problem of resonance-based underwater acoustic absorbers, while the latter makes a pioneering step in reducing the thickness of the absorber without losing the broadband absorption performance. The absorption performance of a large-size sample was verified by measurements in a water pool, with an averaged absorption of 90.3% from 4 kHz to at least 20 kHz. The materials and the design methodology adopted in this work may provide a new route in designing versatile devices with broadband features, such as camouflage stealth materials (*2*, *3*, *54*), tunable waveguides (*55*, *56*), metamaterial-based lens (*8*, *57*, *58*), impedance transformer (*59*, *60*), etc.

MATERIALS AND METHODS

Sample fabrication and characterization

The composite materials were fabricated by using the ingredients described in Fig. 2 of the main text. The Young's modulus of the PU resin (Type Smooth-On Task 6) is 1×10^9 Pa, and that of the PU rubber (Type Smooth-On Simpact 85A) is much softer with a value of 6.83×10^6 Pa. The process of mould making and demoulding can be found in the Supplementary Materials, text S4. The composite sample was fabricated into the long strip geometry (see Fig. 2B) for the tensile test. The tensile equipment we used is Electronic Universal Testing Machine WDW-10 from Jinan Jinyinfeng Instrument Company. The stainless-steel base of the large-scale sample (for the purpose of achieving longitudinal wave reflection) was precisely fabricated using the wire electrical discharge machining. The averaged thickness of the base with the stepped surfaces is 0.06 m, so that the transmitted wave beyond 4 kHz can be significantly suppressed. The density of the stainless steel is 7.5 g/cm^3. By combining the mass of composite rods with the base, the total mass of the sample is around 420 kg. The Young's modulus of the soft glue is in the order of 10^5 Pa, with a negligible shear modulus.

Simulation methods and setups

In numerical simulations, the commercial software COMSOL Multiphysics was adopted for efficient computation. The static pressure test in Fig. 1A was simulated by the Solid Mechanics module. For the simulations involving the evaluation of absorption, the Solid Mechanics module was combined with the Pressure Acoustics module. The former was responsible for the domain of composite rods, and the latter was responsible for the water domain. For the solid-fluid interfaces, continuity boundary conditions were applied for the displacement and stress fields. The lateral boundaries of the simulation domain were set to be the Floquet periodic boundary condition. The four side walls of the composite rods were applied with free boundary condition for the simulation whose results are shown in Fig. 3 (D and E), as an approximation. However, for Fig. 4E, the air gaps were occupied by the acoustic domain, and the free boundaries were replaced by the solid-air interface. In addition, the air gaps and the water are gapped by a thin layer of soft glue with Young's modulus to be ~10^5 Pa. Meanwhile, the stainless-steel base and the water domain at the back side were also added for collecting the transmission information. The mesh size was set to be smaller than one-sixth of a wavelength in order to ensure accuracy.

Water pool measurements

We adopted the time-domain approach to measure the transmission and reflection coefficients in a water pool. A pistonic piezoelectric underwater emitter (Lubell Type 9162 T) was used for wave generation, while an omnidirectional hydrophone (Brüel & Kjaer Type 8105), associated with a signal amplifier conditioner (Nexus Type 2692), was used as receiver. A signal burst windowed by a Hanning function was sent to the source. Each group of the measured signals was averaged 300 times to improve the signal-to-noise ratio. To handle the parasitic echoes coming from multiple reflections on the walls of the pool, we used the following procedures: Measurements were done in the water tank at two positions P1 (front side) and P2 (back side). For each frequency, we carried out the two groups of measurements (i.e., with and without the sample) and then collected the data at P1 and P2. The data without the sample act as the reference signals $S_{\mathrm{ref-P1}}$ (including the incident wave and spurious signals from the reflections by pool walls) and $S_{\mathrm{ref-P2}}$ (approximately treated as the incident signal strength). With the sample present, the signals at P1 and P2 are denoted by S_{P1} and S_{P2}, respectively. Therefore, after projecting the signals into the frequency domain by Fourier transform, we can calculate the reflectance $R = |(S_{\mathrm{P1}} - S_{\mathrm{ref-P1}})/S_{\mathrm{ref-P2}}|^2$ and the transmittance $T = |S_{\mathrm{P2}}/S_{\mathrm{ref-P2}}|^2$.

SUPPLEMENTARY MATERIALS

Supplementary material for this article is available at https://science.org/doi/10.1126/sciadv.abm4206

REFERENCES AND NOTES

1. D. Lee, Y. Jang, J. Park, I. S. Kang, J. Li, J. Rho, Underwater stealth metasurfaces composed of split-orifice–conduit hybrid resonators. *J. Appl. Phys.* **129**, 105103 (2021).
2. G. Yu, Y. Qiu, Y. Li, X. Wang, N. Wang, Underwater acoustic stealth by a broadband 2-bit coding metasurface. *Phys. Rev. Appl.* **15**, 064064 (2021).
3. Y. Gao, J. Song, S. Li, C. Elowsky, Y. Zhou, S. Ducharme, Y. M. Chen, Q. Zhou, L. Tan, Hydrogel microphones for stealthy underwater listening. *Nat. Commun.* **7**, 12316 (2016).
4. N. Jiménez, V. Romero-García, V. Pagneux, J.-P. Groby, Rainbow-trapping absorbers: Broadband, perfect and asymmetric sound absorption by subwavelength panels for transmission problems. *Sci. Rep.* **7**, 13595 (2017).
5. M. Yang, S. Chen, C. Fu, P. Sheng, Optimal sound-absorbing structures. *Mater. Horiz.* **4**, 673–680 (2017).
6. M. Yang, P. Sheng, Sound absorption structures: From porous media to acoustic metamaterials. *Annu. Rev. Mat. Res.* **47**, 83–114 (2017).
7. J. Li, W. Wang, Y. Xie, B.-I. Popa, S. A. Cummer, A sound absorbing metasurface with coupled resonators. *Appl. Phys. Lett.* **109**, 091908 (2016).
8. S. Zhang, C. Xia, N. Fang, Broadband acoustic cloak for ultrasound waves. *Phys. Rev. Lett.* **106**, 024301 (2011).

9. Y. Jin, R. Kumar, O. Poncelet, O. Mondain-Monval, T. Brunet, Flat acoustics with soft gradient-index metasurfaces. *Nat. Commun.* **10**, 143 (2019).
10. V. Leroy, A. Strybulevych, M. Lanoy, F. Lemoult, A. Tourin, J. H. Page, Superabsorption of acoustic waves with bubble metascreens. *Phys. Rev. B* **91**, 020301 (2015).
11. P. S. Wilson, R. A. Roy, W. M. Carey, An improved water-filled impedance tube. *J. Acoust. Soc. Am.* **113**, 3245–3252 (2003).
12. M. Oblak, M. Pirnat, M. Boltežar, An impedance tube submerged in a liquid for the low-frequency transmission-loss measurement of a porous material. *Appl. Acoust.* **139**, 203–212 (2018).
13. D. Zhao, H. Zhao, H. Yang, J. Wen, Optimization and mechanism of acoustic absorption of Alberich coatings on a steel plate in water. *Appl. Acoust.* **140**, 183–187 (2018).
14. J. Wen, H. Zhao, L. Lv, B. Yuan, G. Wang, X. Wen, Effects of locally resonant modes on underwater sound absorption in viscoelastic materials. *J. Acoust. Soc. Am.* **130**, 1201–1208 (2011).
15. Y. Zhang, J. Pan, K. Chen, J. Zhong, Subwavelength and quasi-perfect underwater sound absorber for multiple and broad frequency bands. *J. Acoust. Soc. Am.* **144**, 648–659 (2018).
16. C. Yu, M. Duan, W. He, F. Xin, T. Lu, Underwater anechoic layer with parallel metallic plate insertions: Theoretical modelling. *J. Micromech. Microeng.* **31**, 074002 (2021).
17. L. B. Wang, C. Z. Ma, J. H. Wu, A thin meta-structure with multi-order resonance for underwater broadband sound absorption in low frequency. *Appl. Acoust.* **179**, 108025 (2021).
18. H. Wu, H. Zhang, C. Hao, Reconfigurable spiral underwater sound-absorbing metasurfaces. *Extreme Mech. Lett.* **47**, 101361 (2021).
19. Y. Gu, H. Long, Y. Cheng, M. Deng, X. Liu, Ultrathin composite metasurface for absorbing subkilohertz low-frequency underwater sound. *Phys. Rev. Appl.* **16**, 014021 (2021).
20. J. Zhong, H. Zhao, H. Yang, Y. Wang, J. Yin, J. Wen, Theoretical requirements and inverse design for broadband perfect absorption of low-frequency waterborne sound by ultrathin metasurface. *Sci. Rep.* **9**, 1181 (2019).
21. M. Duan, C. Yu, F. Xin, T. J. Lu, Tunable underwater acoustic metamaterials via quasi-Helmholtz resonance: From low-frequency to ultra-broadband. *Appl. Phys. Lett.* **118**, 071904 (2021).
22. J. Mei, X. Zhang, Y. Wu, Ultrathin metasurface with high absorptance for waterborne sound. *J. Appl. Phys.* **123**, 091710 (2018).
23. Y. Fu, J. Fischer, K. Pan, G. H. Yeoh, Z. Peng, Underwater sound absorption properties of polydimethylsiloxane/carbon nanotube composites with steel plate backing. *Appl. Acoust.* **171**, 107668 (2021).
24. H. Jiang, Y. Wang, Phononic glass: A robust acoustic-absorption material. *J. Acoust. Soc. Am.* **132**, 694–699 (2012).
25. Y. Gu, H. Zhong, B. Bao, Q. Wang, J. Wu, Experimental investigation of underwater locally multi-resonant metamaterials under high hydrostatic pressure for low frequency sound absorption. *Appl. Acoust.* **172**, 107605 (2021).
26. B. Yuan, W. Jiang, H. Jiang, M. Chen, Y. Liu, Underwater acoustic properties of graphene nanoplatelet-modified rubber. *J. Reinforced Plastics Compos.* **37**, 609–616 (2018).
27. J. Heng, Z. Mi-Lin, W. Yu-Ren, H. Yan-Ping, L. Ding, W. Bing-Chen, A wide band strong acoustic absorption in a locally network anechoic coating. *Chin. Phys. Lett.* **26**, 106202 (2009).
28. H. Jiang, Y. Wang, M. Zhang, Y. Hu, D. Lan, Y. Zhang, B. Wei, Locally resonant phononic woodpile: A wide band anomalous underwater acoustic absorbing material. *Appl. Phys. Lett.* **95**, 104101 (2009).
29. H. Meng, J. Wen, H. Zhao, X. Wen, Optimization of locally resonant acoustic metamaterials on underwater sound absorption characteristics. *J. Sound Vib.* **331**, 4406–4416 (2012).
30. L. Li, Z. Zhang, Q. Huang, S. Li, A sandwich anechoic coating embedded with a micro-perforated panel in high-viscosity condition for underwater sound absorption. *Compos. Struct.* **235**, 111761 (2020).
31. Y. Zhang, K. A. Chen, X. Hao, Y. Cheng, A review of underwater acoustic metamaterials. *Chin. Sci. Bull.* **65**, 1396–1410 (2020).
32. G. Ma, C. Fu, G. Wang, P. del Hougne, J. Christensen, Y. Lai, P. Sheng, Polarization bandgaps and fluid-like elasticity in fully solid elastic metamaterials. *Nat. Commun.* **7**, 1356 (2016).
33. Y. Fu, I. I. Kabir, G. H. Yeoh, Z. Peng, A review on polymer-based materials for underwater sound absorption. *Polym. Test.* **96**, 107115 (2021).
34. V. Jayakumari, R. Shamsudeen, R. Rajeswari, T. Mukundan, Viscoelastic and acoustic characterization of polyurethane-based acoustic absorber panels for underwater applications. *J. Appl. Polym. Sci.* **136**, 47165 (2019).
35. P. Sheng, *Introduction to Wave Scattering, Localization and Mesoscopic Phenomena* (Springer Science & Business Media, 2006), vol. 88.
36. L. Adair, R. Cook, Acoustic properties of Rho-C rubber and ABS in the frequency range 100-kHz-2 MHz. *J. Acoust. Soc. Am.* **54**, 1763–1765 (1973).
37. R.-M. Guillermic, M. Lanoy, A. Strybulevych, J. H. Page, A PDMS-based broadband acoustic impedance matched material for underwater applications. *Ultrasonics* **94**, 152–157 (2019).
38. S. Qu, P. Sheng, Minimizing indoor sound energy with tunable metamaterial surfaces. *Phys. Rev. Appl.* **14**, 034060 (2020).
39. T. Gamelin, *Complex Analysis* (Springer Science & Business Media, 2003).
40. M. Yang, P. Sheng, An integration strategy for acoustic metamaterials to achieve absorption by design. *Appl. Sci.* **8**, 1247 (2018).
41. J. D. Jackson, Classical electrodynamics. *Am. Instit. Phys.* **15**, 62–62 (2009).
42. K. N. Rozanov, Ultimate thickness to bandwidth ratio of radar absorbers. *IEEE Trans. Antennas Propagation* **48**, 1230–1234 (2000).
43. S. Qu, Y. Hou, P. Sheng, Conceptual-based design of an ultrabroadband microwave metamaterial absorber. *Proc. Natl. Acad. Sci. U.S.A.* **118**, e2110490118 (2021).
44. F. Kerr, A. Baird, *IUTAM Symposium on Diffraction and Scattering in Fluid Mechanics and Elasticity* (Springer, 2002), pp. 123–132.
45. M. E. Curd, N. F. Morrison, M. J.-A. Smith, P. Gajjar, Z. Yousaf, W. J. Parnell, Geometrical and mechanical characterisation of hollow thermoplastic microspheres for syntactic foam applications. *Compos. Part B Eng.* **223**, 108952 (2021).
46. M. R. Haberman, Y. H. Berthelot, J. Jarzynski, M. Cherkaoui, Micromechanical modeling of viscoelastic voided composites in the low-frequency approximation. *J. Acoust. Soc. Am.* **112**, 1937–1943 (2002).
47. S. M. Ivansson, Numerical design of Alberich anechoic coatings with superellipsoidal cavities of mixed sizes. *J. Acoust. Soc. Am.* **124**, 1974–1984 (2008).
48. G. Ma, M. Yang, S. Xiao, Z. Yang, P. Sheng, Acoustic metasurface with hybrid resonances. *Nat. Mater.* **13**, 873–878 (2014).
49. N. Jiménez, W. Huang, V. Romero-García, V. Pagneux, J.-P. Groby, Ultra-thin metamaterial for perfect and quasi-omnidirectional sound absorption. *Appl. Phys. Lett.* **109**, 121902 (2016).
50. A. Bretagne, A. Tourin, V. Leroy, Enhanced and reduced transmission of acoustic waves with bubble meta-screens. *Appl. Phys. Lett.* **99**, 221906 (2011).
51. J.-P. Groby, R. Pommier, Y. Aurégan, Use of slow sound to design perfect and broadband passive sound absorbing materials. *J. Acoust. Soc. Am.* **139**, 1660–1671 (2016).
52. J.-P. Groby, W. Huang, A. Lardeau, Y. Aurégan, The use of slow waves to design simple sound absorbing materials. *J. Appl. Phys.* **117**, 124903 (2015).
53. N. Jiménez, V. Romero-García, V. Pagneux, J.-P. Groby, Quasiperfect absorption by subwavelength acoustic panels in transmission using accumulation of resonances due to slow sound. *Phys. Rev. B* **95**, 014205 (2017).
54. H. Yuk, S. Lin, C. Ma, M. Takaffoli, N. X. Fang, X. Zhao, Hydraulic hydrogel actuators and robots optically and sonically camouflaged in water. *Nat. Commun.* **8**, 14230 (2017).
55. N. Gao, S. Qu, L. Si, J. Wang, W. Chen, Broadband topological valley transport of elastic wave in reconfigurable phononic crystal plate. *Appl. Phys. Lett.* **118**, 063502 (2021).
56. N. Gao, J. Li, R. Bao, W. Chen, Harnessing uniaxial tension to tune Poisson's ratio and wave propagation in soft porous phononic crystals: An experimental study. *Soft Matter* **15**, 2921–2927 (2019).
57. X. Su, A. N. Norris, C. W. Cushing, M. R. Haberman, P. S. Wilson, Broadband focusing of underwater sound using a transparent pentamode lens. *J. Acoust. Soc. Am.* **141**, 4408–4417 (2017).
58. A. Allam, K. Sabra, A. Erturk, 3D-printed gradient-index phononic crystal lens for underwater acoustic wave focusing. *Phys. Rev. Appl.* **13**, 064064 (2020).
59. E. Dong, Z. Song, Y. Zhang, S. G. Mosanenzadeh, Q. He, X. Zhao, N. X. Fang, Bioinspired metagel with broadband tunable impedance matching. *Sci. Adv.* **6**, eabb3641 (2020).
60. E. Bok, J. J. Park, H. Choi, C. K. Han, O. B. Wright, S. H. Lee, Metasurface for water-to-air sound transmission. *Phys. Rev. Lett.* **120**, 044302 (2018).

Acknowledgments: S.Q. wish to thank Z. Dong, W. Ho, Y. Hou, and H. Y. Mak for assistance in the sample fabrication and shipping. S.Q. appreciates the discussion with M. Yang on the integration scheme. N.G. wishes to thank Z. Wang for guidance in the tensile test, W. Wong for the metal base fabrication, and S. Nie for the dynamic mechanical analysis test. A.T. and B.M. thank H. Cahingt for the technical assistance during the experiments. **Funding:** P.S. acknowledges the support of RGC grant A-HKUST601/18 and AoE/P-502/20-3 for this work. J.-P.G. and V.R.-G. acknowledge the support of the ANR-RGC METARoom project (ANR-18-CE08-0021) for this work. **Author contributions:** S.Q. and N.G. contributed equally to this work. P.S. designed the research, conceived the idea, and supervised the project. S.Q. provided the theoretical framework. N.G. experimentally designed and characterized the composite materials. S.Q. and N.G. conducted the simulations and the sample fabrication. J.-P.G. and V.R.-G. supervised the sample shipment and the experiments in the water pool. B.M. and A.T. performed the absorption measurements of the sample in the water pool. All the authors contributed to the data analysis and manuscript preparation. **Competing interests:** S.Q., N.G., and P.S. are inventors on a pending patent related to this work filed by the Hong Kong University of Science and Technology (no. FI-211547-0221, filed 12 June 2021). The authors declare that they have no other competing interests. **Data and materials availability:** All data needed to evaluate the conclusions in the paper are present in the paper and/or the Supplementary Materials.

Submitted 17 September 2021
Accepted 5 April 2022
Published 18 May 2022
10.1126/sciadv.abm4206